SCIENCE CHINA
Chemistry

•ARTICLES•

https://doi.org/10.1007/s11426-024-2534-9

Tuning anionic bands and lattice stability by short-range disorder at nanoscale for ultrastable Co-free Li-rich cathode

Ruiqi Zhao[1,3], Xingchen Song[1,3], Ziheng Zhang[3,4,5], Jinping Zhang[1,3], Chenghao Zheng[1,3], Jie Zhu[1,3], Jie Liu[1,3], Kai Zhang[3,4,5], Yanfeng Ma[1,3], Chenxi Li[1,3], Hongtao Zhang[1,3*] & Yongsheng Chen[1,2,3*]

[1]*The Centre of Nanoscale Science and Technology and Key Laboratory of Functional Polymer Materials, Institute of Polymer Chemistry, College of Chemistry, Nankai University, Tianjin 300071, China*
[2]*State Key Laboratory of Elemento-Organic Chemistry, Nankai University, Tianjin 300071, China*
[3]*Renewable Energy Conversion and Storage Center (RECAST), Nankai University, Tianjin 300071, China*
[4]*Department Key Laboratory of Advanced Energy Materials Chemistry (Ministry of Education), College of Chemistry, Nankai University, Tianjin 300071, China*
[5]*Engineering Research Center of High-efficiency Energy Storage (Ministry of Education), College of Chemistry, Nankai University, Tianjin 300071, China*

Received November 23, 2024; accepted January 18, 2025; published online February 24, 2025

Ordered layered honeycomb structures are crucial for the unique redox mechanism in Co-free Li-rich oxide materials (LMNO). However, oxygen release and irreversible cation migration originating from this distinctive structure during cycling have hindered the further commercialization of LMNO. Herein, we report a strategy to modulate the nanoscale atomic arrangement and electronic band structures by deliberately introducing an integrated short-range disorder in the Li-rich structure with Ce/F dual-doping (denoted as LMNO-CFSD). This work explicitly reveals the induction of this disordered structure and comprehensively investigates its effects on the lattice stability. As a result, the LMNO-CFSD cathode exhibits a high energy density of 934.8 Wh $kg_{cathode}^{-1}$, and achieves a remarkable lifespan of 800 cycles with 70.1% capacity retention at 1 C in LMNO-CFSD|| graphite full cells. Spectroscopic studies corroborated by first-principles calculations reveal that this integrated short-range disorder with dual-doping effectively modulates the formation energy of oxygen vacancies. It also tailors the crystal and anionic band structure in the Li-rich phase, fundamentally mitigating detrimental oxygen release and transition metal migration during Li^+ (de)intercalation. Our findings illuminate the crucial role of correlated disorder in enhancing the electrochemical properties of Li-rich layered oxides, thereby offering new design principles for high-performance cathode materials in next-generation lithium batteries.

Co-free Li-rich cathode, short-range disorder, anionic band structure, lithium-ion battery

Citation: Zhao R, Song X, Zhang Z, Zhang J, Zheng C, Zhu J, Liu J, Zhang K, Ma Y, Li C, Zhang H, Chen Y. Tuning anionic bands and lattice stability by short-range disorder at nanoscale for ultrastable Co-free Li-rich cathode. *Sci China Chem*, 2025, 68, https://doi.org/10.1007/s11426-024-2534-9

1 Introduction

The development of high-energy-density and low-cost lithium-ion batteries (LIBs) is crucial for advancing a sustainable society powered by various electrified devices. As cathode materials limit the performance of current LIBs, developing the next-generation cathodes has become a primary concern [1]. Li-rich layered oxides (LRLO), with their exceptional energy density exceeding 900 Wh kg^{-1} derived from a unique ordered honeycomb Li-rich phase, are con-

*Corresponding authors (email: htzhang@nankai.edu.cn; yschen99@nankai.edu.cn)

sidered as the most promising cathode materials [2]. Eliminating cobalt from LRLO not only reduces cost but also enhances environmental sustainability, which is typically represented by the formula of $x\mathrm{Li_2MnO_3}\cdot(1-x)\mathrm{LiTMO_2}$ (TM (transition metal) = Mn, Ni). However, the oxidation of O^{2-} in the Li-rich lattice can lead to irreversible oxygen release, structural degradation, and voltage decay, resulting in poor electrochemical performance. These issues have so far hindered the practical application of Co-free LRLO material [3].

Due to the limited structure stability originating from the Li_2MnO_3 lattice, cation arrangement modulation was first considered in enhancing the electrochemical properties of cathode materials. In LRLO, intralayer Li/TM disorder in *R*-3*m* lattice has been shown to relieve lattice strain and promote structural reversibility during cycling [4,5]. Furthermore, chemical short-range disorder, characterized by the localized distribution of elements involving interlayer Li/TM mixing, has been found to prevent structural deterioration in conventional layered oxides like $LiCoO_2$ and $LiNi_{0.8}Mn_{0.1}Co_{0.1}O_2$ [6]. These indicate the potential of the cation arrangement engineering in oxide cathodes. Moreover, strategic formulation of Li/TM arrangement in the Li_2MnO_3 phase has been found to effectively alleviate voltage hysteresis by affecting the local environment around O^{2-} and O redox behavior [7]. An increase in the intralayer cation-disorder in Li_2MnO_3 leads to improved cycle stability [8,9]. Therefore, as the Li-rich coordination environment is the origin of high electrochemical performances yet faces significant challenges, we have aimed to modify the local atomic arrangement of the Li-rich coordination structure at the nanometer scale to regulate the unique O 2p lone pairs (*l*O2p) activity beyond the abovementioned intralayer cation-disorder [10].

To address the above-mentioned challenges, foreign element doping has also been prevailing for structural modification [11]. This approach involves incorporating dopants into the parent lattice to regulate the intrinsic properties of the material [12]. Based on empirical studies, we have established several criteria for selecting appropriate dopants: (1) enhancing lattice oxygen stability through stronger covalent bonding, (2) mitigating TM ion migration during cycling, and (3) inducing an appropriate degree of Li/TM mixing through atomic rearrangement to achieve a short-range disorder, especially in the Li_2TMO_3 structure [13,14]. Among the potential dopants, Ce^{4+} cation, possessing higher bond energy and covalency with O compared to Mn–O and Ni–O, can effectively modulate the local electronic structure of the oxygen atoms [15]. Its d^0 electronic configuration also tends to promote a disordered phase in a Li-rich environment, thus regulating Li/TM mixing and atomic arrangement [16,17]. Additionally, F^- anion with higher electronegativity can enhance overall structure stability and is thermodynamically favored in disordered rocksalt-type transition metal oxides [18,19]. Therefore, small amounts of Ce^{4+} and F^- are introduced as dopants to facilitate an optimal level of Li/TM mixing for the short-range disorder, as well as stabilize the crystalline lattice of LRLO during cycling.

Herein, we propose a strategy to introduce a short-range disorder at the nanoscale in the Li-rich coordination structure through Ce/F dual-doping to modify $Li_{1.2}Mn_{0.6}Ni_{0.2}O_2$ (LMNO) lattice, successfully synthesizing $Li_{1.2}Mn_{0.6}Ni_{0.2}Ce_{0.004}O_2F_{0.016}$ (LMNO-CFSD). This disorder structure is induced by Ce cation and F anion doping and featured by localized element arrangements with interlayer cation intermingling, thus enhancing the intrinsic stability of LNMO-CFSD. The synergistic effects of this short-range disorder and dual-doping strategy effectively modulate the O 2p bands and refine both crystal and electronic configurations, fundamentally mitigating oxygen release, TM migration and structural degradation during cycling. Consequently, in coin-type full cells paired with graphite, LMNO-CFSD cathode exhibits exceptional electrochemical performance with a high gravimetric energy density of 934.8 Wh kg^{-1} under 0.1 C and a capacity retention of 70.1% after 800 prolonged cycles under 1 C. Additionally, the LMNO-CFSD||graphite quasi-solid-state LIBs in coin-type cells demonstrate a superior lifespan of 400 cycles with 72.0% capacity retention. Our findings provide valuable insights into the regulation of cation arrangements and intrinsic properties of the Li_2TMO_3 lattice in Li-rich layered oxides, potentially paving the way for the development of high-performance cathode materials for next-generation lithium batteries.

2 Results and discussion

2.1 Materials synthesis and structural characterization

LMNO-CFSD was prepared by a typical co-precipitation technique followed by subsequent solvothermal and solid-state calcination methods, with a small amount of Ce/F added (details in the Supporting Information online). For comparison, a controlled LMNO and LMNO doped by different ratios of Ce or F (denoted as LMNO-Ce and LMNO-F) were obtained via similar procedures without the addition of Ce or F. Firstly, the morphologies of LMNO and LMNO-CFSD particles were examined using field emission scanning electron microscopy (FESEM) (Figure S1 Supporting Information online). Both materials consist of small, irregularly shaped polyhedral primary particles with an average size of around 150 nm.

Powder X-ray diffraction (p-XRD) was then employed to verify the structures of LMNO-CFSD, the controlled LMNO, LMNO-Ce and LMNO-F, which are presented in Figure 1a, Figures S2 and S3. The Rietveld refinement results with crystallographic sites in Tables S1 and S2 (Supporting Information online) confirm that both the LMNO-CFSD and controlled LMNO exhibit characteristic diffrac-

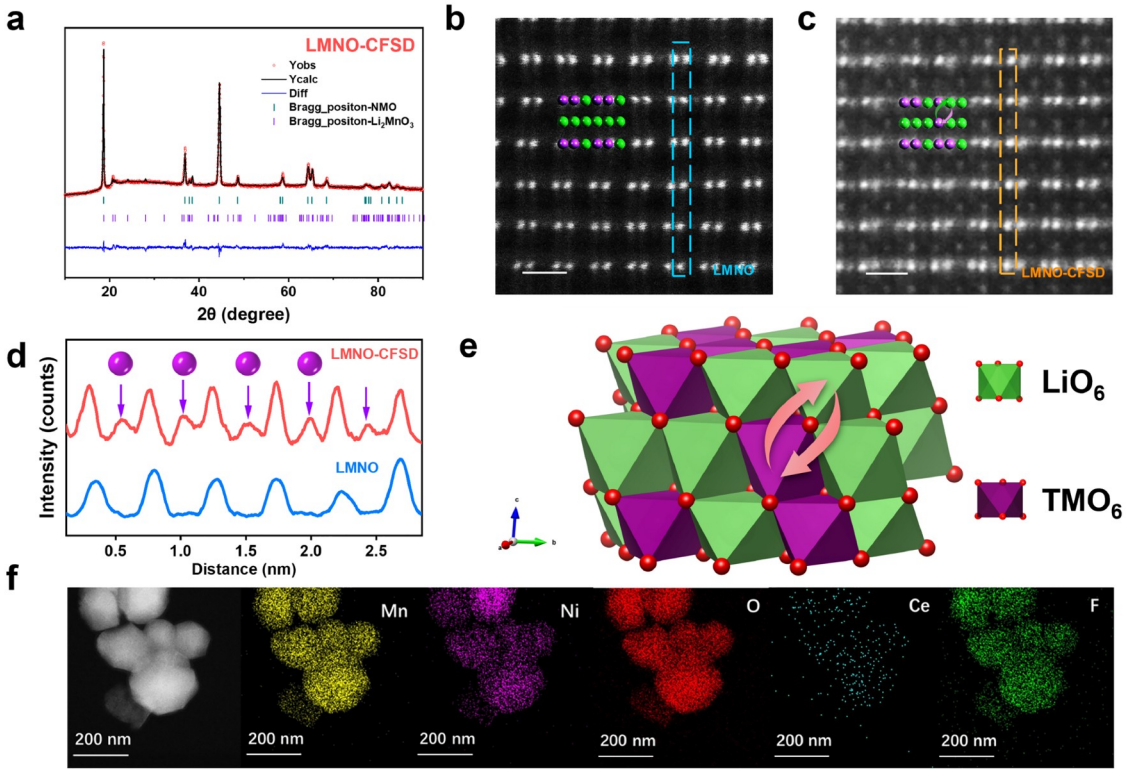

Figure 1 (Color online) (a) Rietveld refinement of the p-XRD pattern of LMNO-CFSD. HAADF-STEM images of (b) the controlled LMNO and (c) LMNO-CFSD particles. Scale bars, 0.5 nm. (d) Line profiles along the vertical direction of the selected regions in (b) and (c). (e) Schematic crystal structure of the corresponding short-range disorder with interlayer cation intermingling. (f) TEM-EDS mapping images of LMNO-CFSD.

tion reflections corresponding to the α-$NaFeO_2$ structure with *R*-3*m* space group and a monoclinic Li_2MnO_3 phase with *C*2/*m* space group [20]. In LMNO-CFSD, Ce atoms are placed at TM sites and F atoms are replaced with O in the unit cell. Notably, the intensity ratio of (003)/(104) peaks in LMNO-CFSD is lower than that of the controlled LMNO, suggesting a higher disordered degree of LMNO-CFSD material [21]. It is further supported by data in Tables S1 and S2, which indicates an increased degree of Li/Ni mixing from 4% to 8%. Meanwhile, the percentage of the Li_2MnO_3 phase decreases, which implies an increase in structural disorder in the Li-rich phase [10]. To further investigate the lattice configuration, atomic-resolution high-annular dark field scanning transmission electron microscopy (HAADF-STEM) was performed. In Figure 1b, the controlled LMNO shows the typical dumbbell structure indexed to the Li_2TMO_3 lattice [22]. In contrast, the LMNO-CFSD exhibits not only the dumbbell structure but also the distinct contrast in several locations within the Li layer, indicating the presence of TM ions (Figure 1c and Figure S4). This observation aligns with the increased disorder noted in LMNO-CFSD. Line profiles in Figure 1d further illustrate the disorder phenomenon, confirming the short-range disordered configuration with Li/TM interlayer cation intermingling schematically displayed in Figure 1e. It suggests that Ce/F dual-doping can induce Li/Ni mixing in this structure.

Specifically, the d^0 electronic configuration of Ce^{4+} tends to intensify the pseudo Jahn-Teller distortion (PJTE), which is one of the major interactions responsible for generating disorder in TM oxides. This distortion enables Ce^{4+} to displace from the octahedral center, thereby mitigating the distortion caused by the significant charge disparity between Li and the TMs [5]. In another aspect, F^- ions are preferentially coordinated with Li ions in the TM layer, which is probably due to their electronic configuration and outstanding electronegativity. This preference indicates that the formation of more Li–F bonds is energetically more favorable than that of TM–F [23]. Thus, the formation energy of the crystal decreases when F bonded Ni ions are replaced by adjacent Li to form Li–F bonds [19]. This implies that Li/TM mixing is thermodynamically permitted near the substituted F sites. Hence, the introduction of F^- can also reduce the Li/TM mixing energy, promoting the formation of a disordered phase. To further confirm these findings, density functional theory (DFT) calculations were employed to investigate the formation mechanism of this short-range disorder. As demonstrated in Figure S5, Ce/F dual-doping effectively reduces the Li/TM (specifically assumed to be Ni) mixing energy to 2.30 eV in LMNO-CFSD, compared to 2.92 eV in the controlled LMNO. This reveals that Ce/F dual-doping facilitates the formation of short-range disorder during synthesis by promoting a small amount of Li/TM mixing.

Moreover, to verify the elemental distributions, energy-dispersive X-ray spectroscopy (EDS) was conducted for LMNO-CFSD. As displayed in Figure 1f, the main elements Mn, Ni, and O along with a small amount of Ce, F, are uniformly distributed in the sample. Additionally, X-ray photoelectron spectroscopy (XPS) analysis was employed to study the valences of Ce, which is assigned to +4 according to the signals at 205–225 eV, as shown in Figure S6 [24]. Meanwhile, the chemical compositions of the controlled LMNO and LMNO-CFSD were confirmed by inductively coupled plasma optical emission spectrometry (ICP-OES) and ion selective electrode (ISE) results (Tables S3 and S4). These results further confirm the composition of $Li_{1.2}Mn_{0.6}Ni_{0.2}Ce_{0.004}O_2F_{0.016}$. Therefore, an integrated short-range disorder structure through Ce/F dual-doping modification was introduced in the LMNO-CFSD.

2.2 Electrochemical performances

The electrochemical performances of LMNO-CFSD, enhanced by the integrated short-range disorder structure with Ce/F dual-doping, were evaluated against the controlled LMNO using coin-type half-cells within a potential range of 2.0–4.8 V (vs. Li/Li^+). The initial galvanostatic charge/discharge profiles at 0.1 C (1 C = 200 mA g^{-1}, following the reported literature [25]) presented in Figure 2a reveal that both materials exhibit similar initial charge capacities with two-step charge profiles. During discharge, LMNO-CFSD

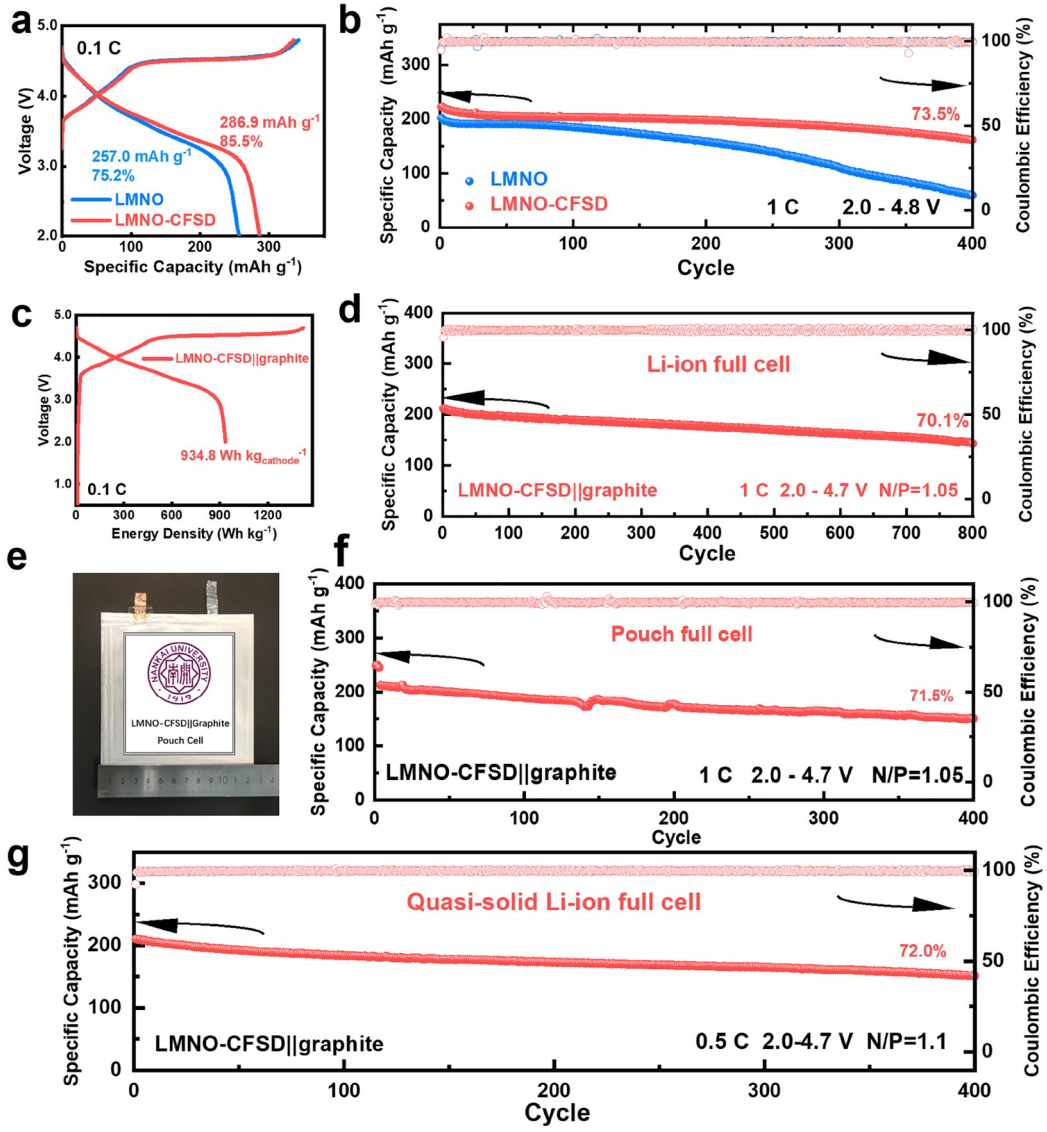

Figure 2 (Color online) Electrochemical performances of LMNO and LMNO-CFSD cathodes. (a) Initial charge-discharge profiles of half cells for both cathodes at 0.1 C. (b) Cycling performances of half cells for both cathodes at 1 C. (c) Initial charge-discharge profiles of LMNO||graphite full cells at 0.1 C. (d) LMNO-CFSD||graphite full cell cycling performances at 1 C. (e) Digital photo of LMNO-CFSD||graphite pouch cell. (f) LMNO-CFSD||graphite pouch cell cycling performances at 1 C. (g) LMNO-CFSD||graphite quasi-solid Li-ion full cell cycling performance at 0.5 C.

delivers a higher reversible capacity of 287.0 mAh g^{-1} at 0.1 C compared to the controlled LMNO (256.7 mAh g^{-1}), leading to a higher initial coulombic efficiency (ICE) of 85.5%. This implies a suppressed irreversible side reaction during the first charge-discharge process. The cycling performance data, shown in Figure 2b, further highlight the benefits of the LMNO-CFSD structure. During 300 cycles at 1 C, LMNO-CFSD demonstrates an initial discharge capacity of 220.7 mAh g^{-1} with an outstanding capacity retention of 80.2%, and still retains 73.5% of its capacity after 400 cycles. In stark contrast, the controlled LMNO shows severe capacity decay, retaining only 28.3% of its discharge capacity after 400 cycles. Meanwhile, the cycling performances of cathodes with different doping ratios Ce/F in Figure S7 also suggest the better cycling performance of LMNO-CFSD. Moreover, the LMNO-CFSD electrode demonstrates better average discharge voltage retention, maintaining a voltage of 3.03 V after the cycle, which is notably 0.56 V higher than that of the controlled LMNO (Figure S8). The voltage decay rate of LMNO-CFSD is significantly lower (1.2 mV per cycle) than that of the controlled LMNO (2.8 mV per cycle). This improved stability of voltage is also evident from the charge-discharge voltage profiles for both cathodes during the 1^{st}, 100^{th}, …, and 400^{th} cycles, as depicted in Figure S9, with the corresponding average discharge voltage values listed in Table S5 [26]. Meanwhile, the rate capabilities of LMNO-CFSD were investigated at various current densities. As shown in Figure S10, LMNO-CFSD demonstrates a reversible specific capacity of 188.8 mAh g^{-1} under 5 C, which is notably higher than that of the controlled LMNO. These results suggest that the strategic incorporation of a short-range disorder with dual-doping in LNMO-CFSD markedly enhances its electrochemical performance.

To further evaluate the performances of LMNO-CFSD in a practical scenario, Li-ion full cells were assembled using LMNO-CFSD cathode paired with graphite anode, operating in a potential window of 2.0–4.7 V (vs. Li/Li^+). In the LMNO-CFSD||graphite coin-type full cells, the LMNO-CFSD cathodes exhibit a high gravimetric energy density of 934.8 Wh kg^{-1} with a discharge capacity of 262.1 mAh g^{-1} (Figure 2c and Figure S11) [27]. As illustrated in Figure 2d, the full cells demonstrate a remarkable lifespan of 500 cycles with an impressive capacity retention of 80.2%, and retain 70.1% capacity even after 800 cycles under 1 C. This performance ranks among the most exceptional cycling results for Li-ion full cells using LRLO cathodes (Table S6). The average voltage attenuation rate per cycle of LMNO-CFSD is only 0.7 mV (Figure S12). When increasing the mass-loading up to 2 mAh cm^{-2} (with N/P = 1.05), the LMNO-CFSD coin-type full cell still exhibits excellent durability, remaining 84.2% of its discharge capacity after 150 cycles under 0.5 C (Figure S13). It achieves a high energy density of 316 Wh kg^{-1} based on the total weight of electrodes, separator and electrolyte (details in Table S7). Meanwhile, the LMNO-CFSD||graphite pouch cells were also constructed (Figure 2e and Figure S14), exhibiting impressive cycling stability with 71.5% capacity retention after 400 cycles at 1 C (Figure 2f). Moreover, LMNO-CFSD||Si-C coin-type full cells were assembled and tested with a potential window of 2.0–4.55 V (vs. Li/Li^+), which retained 67.8% capacity after 400 cycles under 0.5 C (Figure S15). Addressing industry safety concerns, quasi-solid-state batteries were also fabricated with LMNO-CFSD cathodes [28]. As shown in Figure 2g, the LMNO-CFSD||graphite quasi-solid Li-ion full cells exhibit an exceptional cycling performance during 400 cycles with a capacity retention of 72.0% under 0.5 C. Furthermore, in configurations using ultrathin Li-foil anodes (20 μm) and 1.6 mAh cm^{-2} LMNO-CFSD cathodes (N/P = 2), the coin-type quasi-solid Li-metal full batteries achieve a discharge capacity of 249.5 mAh g^{-1} at 0.1 C and retain 81.0% capacity after 50 cycles at 0.3 C (Figure S16). These extensive testing scenarios confirm the high-capacity retention and versatility of LMNO-CFSD across various battery configurations and operational conditions, highlighting the promising potential of LMNO-CFSD for practical application.

2.3 Oxygen behaviour and structural evolution

Considering the outstanding electrochemical performances of LMNO-CFSD compared to the controlled LMNO, *in situ* measurements were conducted on both materials for mechanism studies. To assess the surface oxygen stability, *operando* differential electrochemical mass spectrometry (DEMS) measurements were carried out to monitor O_2 gas evolution during the high-voltage charging of Li_2MnO_3 activation in the first cycle. Figure 3a, b show that the amount of O_2 generated from LMNO-CFSD is significantly reduced to 2.7 nmol g^{-1}, presenting an 84.2% decrease compared to the controlled LMNO (17.1 nmol g^{-1}). This substantial reduction in oxygen release demonstrates the effectiveness of the short-range disorder with dual-doping in mitigating oxygen evolution.

To further study the structural evolution discrepancies between LMNO-CFSD and the controlled LMNO, *in situ* XRD analysis was conducted during the first two cycles. Contour plots of the three characteristic diffraction peaks of $(003)_R$, $(020)_C$ and $(101)_R$ planes for LMNO-CFSD and the controlled LMNO are displayed in Figure 3c, d respectively, with the corresponding charge-discharge profiles on the left. For both samples, the diffraction peaks $(003)_R$ shift to a lower 2θ degree at the onset of the first charge. This shift is attributed to the enhanced electrostatic repulsion between adjacent oxygen layers, which is consistent with the increased lattice parameter c in Figure 3e [29]. Meanwhile, the $(101)_R$

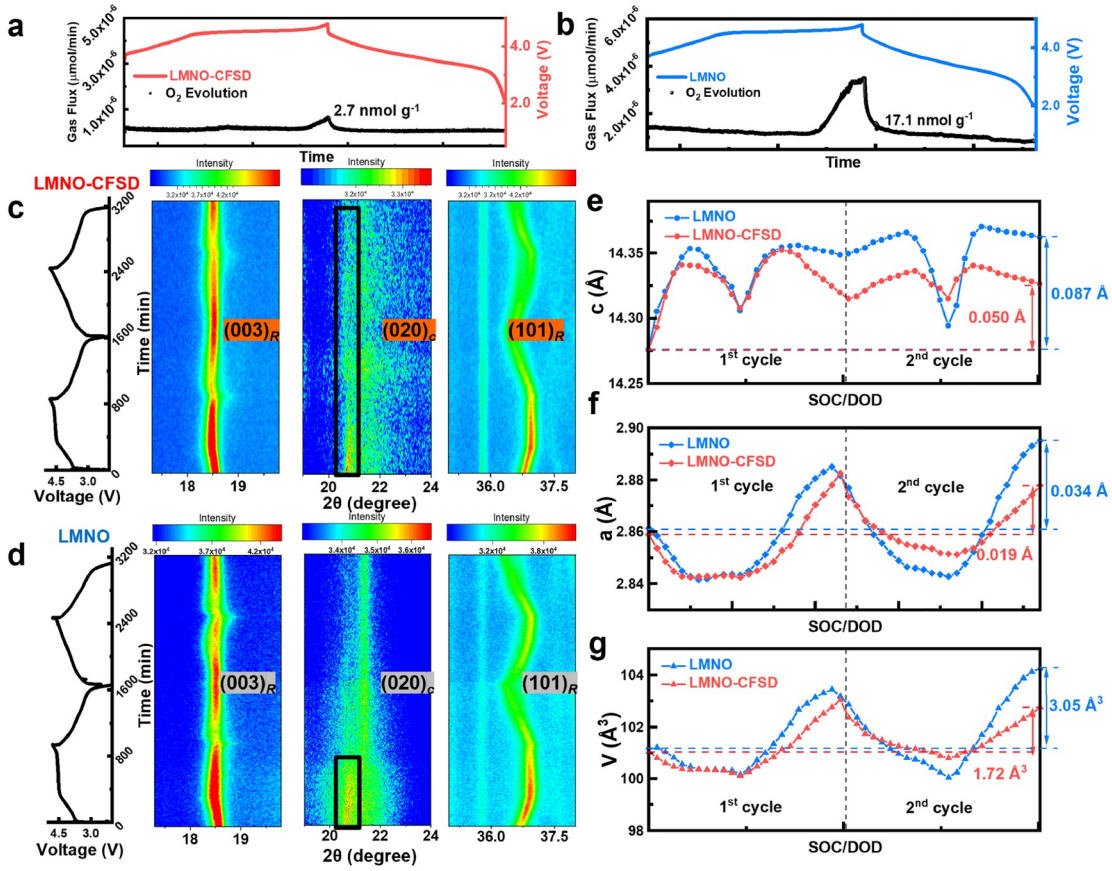

Figure 3 (Color online) DEMS of (a) LMNO-CFSD and (b) the controlled LMNO collected during initial galvanostatic charge/discharge. Contour plots of the *in situ* XRD patterns for (c) LMNO-CFSD and (d) the controlled LMNO with the voltage profiles. Evolution of refined lattice parameters (e) *c*, (f) *a*, and (g) cell volumes obtained by XRD patterns during the initial two charge/discharge process for both samples.

peaks shift to a higher degree resulting from the shortened TM–O bond during TM oxidation, which is in line with the decreased parameter *a* in Figure 3f. With the voltage rapidly reaching 4.8 V, the $(003)_R$ peaks drastically shift to a higher angle, accompanied by an abrupt drop in *c*-parameters, which is associated with irreversible oxygen loss and subsequent structural degradation with TM migration [30]. During the lithiation process, the lattice parameters shift with trends opposite to those observed during de-lithiation, which can be attributed to the Li^+ re-intercalation and the cationic reduction. The lattice parameters during the second charge-discharge process change analogous to the first cycle. After two cycles, the parameters *a* and *c* for the controlled LMNO drastically changed by 0.034 and 0.079 Å respectively. In contrast, these changes are significantly suppressed to 0.022 and 0.046 Å in LMNO-CFSD. Consequently, the cell volume expansion of LMNO-CFSD has been effectively mitigated to 1.89 $Å^3$ compared to 2.95 $Å^3$ for the controlled LMNO (Figure 3g). Therefore, a relatively smaller lattice variation has been achieved due to the integrated short-range disorder structure with dual-doping modification. More importantly, throughout the charging process for both samples, the $(020)_C$ peak intensities of Li_2MnO_3 decreased, indicating the activation and structural distortion of the Li-rich coordination structure. By the end of the second cycle, the $(020)_C$ peaks of LMNO-CFSD still preserve a certain level of intensity, which are nearly extinguished in the controlled LMNO. This suggests that the structural deterioration of the Li_2MnO_3 phase during cycling has been effectively mitigated through structure modulation. In conclusion, the enhanced lattice oxygen stability as well as structural stability of LMNO-CFSD indicates superior structural robustness during cycling compared to the controlled LMNO.

2.4 Investigation of lattice stability by DFT calculations

DFT calculations were employed to investigate the impact of Ce/F dual doping and the incorporation of a short-range disorder on stabilizing the honeycomb structure as well as preventing irreversible oxygen loss. The calculation models with Li-rich coordination for LMNO-CFSD and the controlled LMNO are depicted in Figure 4a, b. Initially, the electronic band structures were analyzed by examining the partial density-of-states (pDOS) of O_{2p} orbitals for both

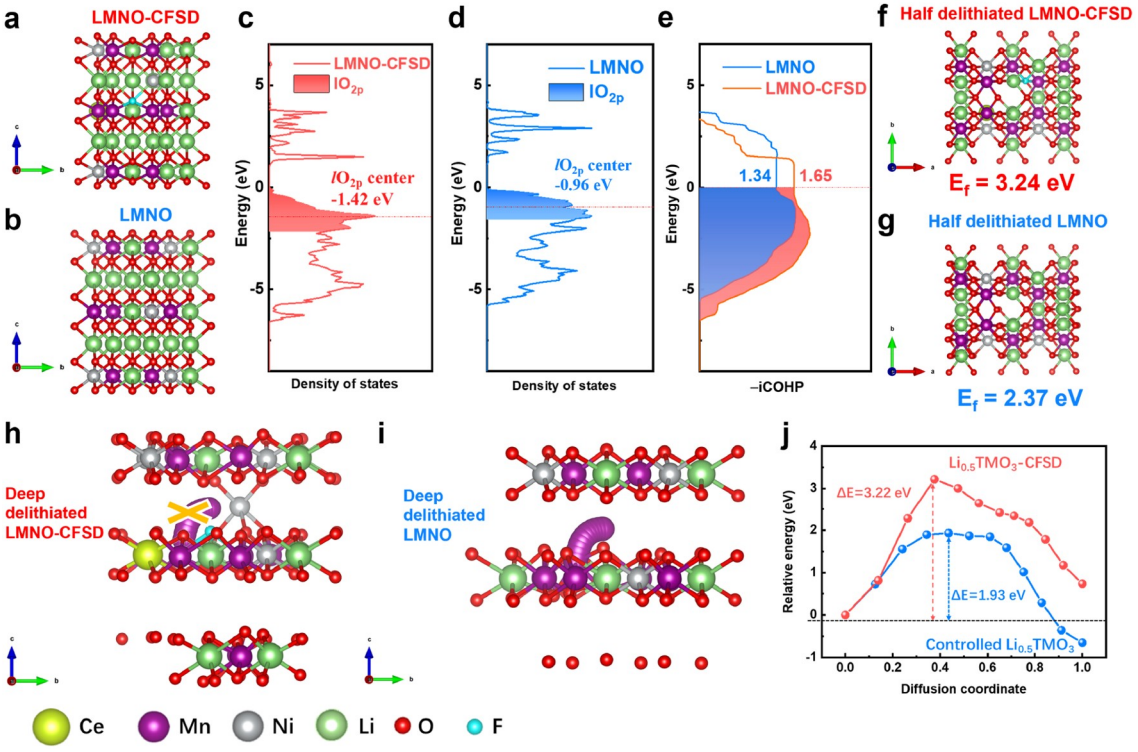

Figure 4 (Color online) Structure models of (a) LMNO-CFSD and (b) the controlled LMNO. The purple spheres are Mn, grey Ni, green Li, red O, yellow Ce, and blue F. Density of states of O-2p states and TM-3d states in (c) LMNO-CFSD and (d) the controlled LMNO. (e) The iCOHP analysis of Mn–O for LMNO-CFSD and the controlled-LMNO. Half de-lithiated models and formation energies of oxygen vacancy for (f) LMNO-CFSD and (g) the controlled LMNO. Mn migration paths in lithium deep-deficient models for (h) LMNO-CFSD and (i) the controlled LMNO. (j) The migration energy barriers of Mn^{4+} to octahedral site in Li layer in deep de-lithiated LMNO-CFSD and the controlled LMNO.

systems during cycling, as illustrated in Figure 4c, d. Detailed examinations focused on the lO_{2p} band, which is crucial for the unique oxygen redox performance by coordinating with two transition metals and four lithium atoms [31]. Assuming the complete de-intercalation of Li^+, one-third of the oxygen electrons will be involved in the electrochemical-active redox. Hence, the lO_{2p} band centers of LMNO-CFSD and the controlled LMNO were calculated as −1.42 and −0.96 eV, respectively, indicating the regulated local electronic structure and improved stability of lone oxygen pair redox in LMNO-CFSD with lower band centers [32]. Meanwhile, the crystal orbital Hamiltonian population (COHP) and integrated COHP (iCOHP) of Mn–O bonds in both cathode materials were calculated to quantitatively evaluate the bonding strength (Figure S17 and Figure 4e) [33]. The calculated iCOHP values at the Fermi energy level correspond to the amount of occupied orbitals in the Mn–O bonds, which is higher in LMNO-CFSD (1.65) compared to that in the controlled LMNO (1.34) [34]. It suggests that the Mn–O bond in LMNO-CFSD is stronger than that in the controlled LMNO. To further study the oxygen stability, the formation energies of oxygen vacancy were computed in the half delithiated models, as shown in Figure 4f, g [35]. The oxygen vacancy in LMNO-CFSD requires a higher formation energy of 3.24 eV than that in the controlled LMNO (2.37 eV). This suggests the improved stability of lattice oxygen in LMNO-CFSD, enhancing the overall durability of the material.

The study of transition metal migration in lithium deep-deficient models is crucial as the reason for structural deterioration during charge-discharge cycles. In the models depicted in Figure 4h, i, Mn ions from the TM layer are shown to migrate to the nearest octahedral Li site in the Li layer both in LMNO-CFSD and the controlled LMNO, which is a key factor in the degradation of the material structure over time. The energy barriers for Mn ion migration are calculated and presented in Figure 4j. For LMNO-CFSD, the migration energy barrier (3.22 eV) is markedly higher compared to that for the controlled LMNO (1.93 eV). This higher energy barrier in LMNO-CFSD suggests that the migration of Mn ions is kinetically slower, which contributes to mitigating the structural degradation that typically occurs during cycling. Meanwhile, at the end of migration, the energy level of the LMNO-CFSD model is apparently higher than that of the controlled LMNO, further indicating the thermodynamically inhibited TM migration in LMNO-CFSD. These findings demonstrate that in LMNO-CFSD, TM migration is suppressed both kinetically and thermodynamically. In a word, an integrated short-range disorder structure with Ce/F dual doping plays an important role in regulating the crystal and

electronic structure of the material, which is consistent with the characterization results with significantly enhanced structural stability during cycling.

2.5 Bulk-to-surface stability during cycling

The improved structural stability of LMNO-CFSD during cycling is further evidenced by *ex situ* HAADF-STEM analysis. In Figure 5a, cycled LMNO-CFSD exhibits a well-preserved layered structure in the bulk, with only a few phase transition layers on the particle surface. These phase transition layers present as a spinel structure in the magnified images shown in Figure 5e (marked by a white dash) [36]. Additionally, electron energy loss spectroscopy (EELS) line-scanning analysis was conducted to further confirm the phase transition area by comparing Mn valence states across different regions from bulk to surface, as depicted in Figure 5b. The Mn-L_3 peaks show slight shifts towards the low energy direction from location D to C, B, A (bulk to surface), which corresponds to the lower Mn valence states in the spinel structure (Mn^{3+} and Mn^{4+}) on the particle surface compared to that in the layered structure (Mn^{4+}) in the bulk [37]. By contrast, phase transition areas are clearly visible both in the bulk and on the particle surface of the cycled controlled LMNO (Figure 5c). These areas also appear to be spinel phase in Figure 5f (marked by a yellow dash), indicating much severe uncontrollable oxygen loss and subsequent structural deterioration compared to LMNO-CFSD, affecting both the surface and the bulk. In Figure 5d, the Mn-L_3 peaks shift to lower energy appears not only at the surface (location A) but also in the bulk (location C). Along with these structural degradations, LMNO typically suffers from severe TM dissolution, which deposits on the anode after the discharge process. Therefore, ICP-MS analysis was performed on the cycled Li anodes to investigate the dissolution of TMs from the cathode materials. As shown in Figure S18, the LMNO-CFSD system exhibits significantly reduced concentrations of Mn and Ni compared to the control LMNO, indicating that TM dissolution was effectively suppressed in the LMNO-CFSD cathode materials. These results directly reveal that the structure deterioration from layered to spinel phase within the particle has been effectively alleviated in LMNO-CFSD after cycling. It indicates that this integrated short-range disorder structure with dual-doping effectively stabilizes crystal lattice during cycling, enhancing the durability and performance of the material.

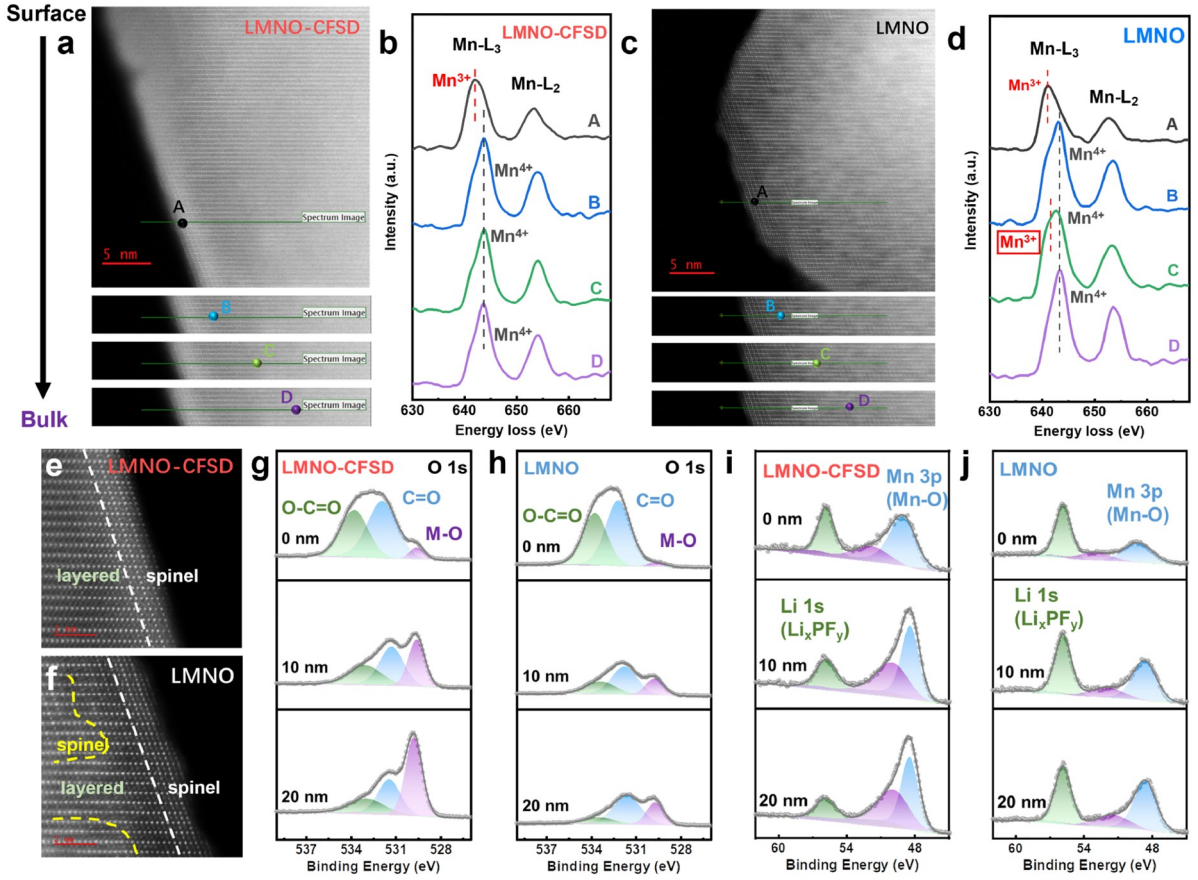

Figure 5 (Color online) STEM images along with EELS line scan regions of (a, b, e) LMNO-CFSD and (c, d, f) the controlled LMNO after 20 cycles. Scale bars, 5 nm in (a, c), 2 nm in (e, f). (g, h) O 1s, (i, j) Li 1s and Mn 3p XPS depth profiles of (g, i) LMNO-CFSD and (h, j) the controlled LMNO after 100 cycles.

Ex situ XPS depth profiling analyses were carried out on the cathodes to systematically study the interfacial stability by detecting chemical compositions of the cathode-electrolyte interface (CEI). On top of the surface, the LMNO-CFSD spectrum displays a more pronounced peak of lattice oxygen (M–O) in the O 1s spectra compared to the controlled LMNO (Figure 5g, h) [38]. Conversely, the intensities of C=O and O–C=O signals at ~532.0 and ~533.8 eV are lower in LMNO-CFSD than those in the controlled LMNO, which are attributed to the less carbonate solvent decomposition [39]. Upon sputtering, the intensities of organic species on the LMNO-CFSD cathode decrease significantly, while M–O peak intensities show an evident increase in O 1s spectra. This suggests the mitigated oxygen loss in the particle as well as fewer side reaction products deposited on the surface of LMNO-CFSD after the cycle [40]. Similarly, as illustrated in Figure 5i, j, the Li 1s peaks at ~55.8 eV and Mn 3p peaks at ~48.3 eV are mainly assigned to lithium salt decomposition products (Li_xPF_y) and the crystal lattice of electroactive cathode materials (Mn–O), respectively [41]. The LMNO-CFSD cathode demonstrates a relatively stronger Mn–O signal compared to the controlled LMNO. With the depth increasing, the Mn–O signal intensities are apparently higher in LMNO-CFSD, while Li_xPF_y peak intensities decrease in Figure 5j. In contrast, the controlled LMNO shows only a slight increase in Mn–O, with Li 1s signals maintaining a high intensity. These results reveal that the interfacial side reactions between LMNO-CFSD and electrolyte have been effectively suppressed, consequently reducing the deposition of the decomposition products [42]. Therefore, owing to the regulated lattice structure and anionic electronic band structure, bulk-to-surface stability has been significantly enhanced by the integrated structural engineering of short-range disordered structure with Ce/F dual doping.

3 Conclusions

In summary, we have successfully synthesized and studied a Co-free Li-rich material featuring an integrated short-range disorder through Ce/F dual-doping. The designed LMNO-CFSD demonstrates exceptional electrochemical performances, with a high energy density of 934.8 Wh kg^{-1} and an excellent capacity retention of 70% after 800 cycles in LMNO-CFSD||graphite full cells under 1 C. Moreover, both pouch and quasi-solid full cells based on LMNO-CFSD cathode deliver capacity retention of over 70% after 400 cycles. Comprehensive mechanism and calculation studies reveal that this excellent performance can be attributed to the optimized crystal and electronic band structure. The synergistic effects of the short-range disorder and dual-doping fundamentally regulate the oxygen vacancy formation energy, mitigate oxygen release, and enhance structural stability during cycling. Our findings highlight the critical role of nanoscale structural engineering in tailoring the atomic arrangements within the Li_2TMO_3 phase, and prompt a re-evaluation of dopant deployment strategies in cathode material design, thus echoing the importance of modulating both local atomic configurations and electronic structures. This strategic atomic arrangement modulation effectively demonstrated advances for the next-generation lithium batteries, achieving both longevity and high energy density.

Acknowledgements This work was supported by the National Natural Science Foundation of China (NSFC, 52090034) and the National Key R&D Program of China (2020YFA0711500).

Conflict of interest The authors declare no conflict of interest.

Supporting information The supporting information is available online at http://chem.scichina.com and http://link.springer.com/journal/11426. The supporting materials are published as submitted, without typesetting or editing. The responsibility for scientific accuracy and content remains entirely with the authors.

1 Huang W, Lin C, Zhang M, Li S, Chen Z, Zhao W, Zhu C, Zhao Q, Chen H, Pan F. *Adv Energy Mater*, 2021, 11: 2102646
2 Murdock BE, Toghill KE, Tapia-Ruiz N. *Adv Energy Mater*, 2021, 11: 2102028
3 Marie JJ, House RA, Rees GJ, Robertson AW, Jenkins M, Chen J, Agrestini S, Garcia-Fernandez M, Zhou KJ, Bruce PG. *Nat Mater*, 2024, 23: 818–825
4 Jiang YS, Liao ZM, Yu FD, Ke W, Li XY, Xia Y, Xu GJ, Sun G, Xia YG, Yin W, Deng L, Zhao L, Wang ZB. *Adv Mater*, 2024, 36: e2404982
5 Kang S, Lee S, Lee H, Kang YM. *Nat Rev Chem*, 2024, 8: 587–604
6 Wang Q, Yao Z, Wang J, Guo H, Li C, Zhou D, Bai X, Li H, Li B, Wagemaker M, Zhao C. *Nature*, 2024, 629: 341–347
7 Zhang M, Qiu L, Hua W, Song Y, Deng Y, Wu Z, Zhu Y, Zhong B, Chou S, Dou S, Xiao Y, Guo X. *Adv Mater*, 2024, 36: 2311814
8 Song J, Ning F, Zuo Y, Li A, Wang H, Zhang K, Yang T, Yang Y, Gao C, Xiao W, Jiang Z, Chen T, Feng G, Xia D. *Adv Mater*, 2023, 35: 2208726
9 Li Y, Xie L, Zheng Z, Yin ZW, Li J, Weng M, Liu J, Hu J, Yang K, Qian G, Cao B, Li Z, Xu S, Zhao W, Li S, Sun J, Zhang M, Pan F. *Nano Energy*, 2020, 77: 105157
10 Jarvis KA, Deng Z, Allard LF, Manthiram A, Ferreira PJ. *Chem Mater*, 2011, 23: 3614–3621
11 Zeng L, Liang H, Qiu B, Shi Z, Cheng S, Shi K, Liu Q, Liu Z. *Adv Funct Mater*, 2023, 33: 2213260
12 Li M, Liu T, Bi X, Chen Z, Amine K, Zhong C, Lu J. *Chem Soc Rev*, 2020, 49: 1688–1705
13 He W, Guo W, Wu H, Lin L, Liu Q, Han X, Xie Q, Liu P, Zheng H, Wang L, Yu X, Peng DL. *Adv Mater*, 2021, 33: 2005937
14 House RA, Rees GJ, Pérez-Osorio MA, Marie JJ, Boivin E, Robertson AW, Nag A, Garcia-Fernandez M, Zhou KJ, Bruce PG. *Nat Energy*, 2020, 5: 777–785
15 Wang L, Liu G, Xu R, Wang X, Wang L, Yao Z, Zhan C, Lu J. *Adv Energy Mater*, 2023, 13: 2203999
16 Zhang C, Feng Y, Wei B, Liang C, Zhou L, Ivey DG, Wang P, Wei W. *Nano Energy*, 2020, 75: 104995
17 Gou X, Hao Z, Hao Z, Yang G, Yang Z, Zhang X, Yan Z, Zhao Q, Chen J. *Adv Funct Mater*, 2022, 32: 2112088
18 Bi Z, Yi Z, Zhang L, Wang G, Zhang A, Liao S, Zhao Q, Peng Z, Song L, Wang Y, Zhao Z, Wei S, Zhao W, Shi X, Li M, Ta N, Mi J, Li S, Das P, Cui Y, Chen C, Pan F, Wu ZS. *Energy Environ Sci*, 2024, 17:

2765–2775
19 Pei Y, Li S, Chen Q, Liang R, Li M, Gao R, Ren D, Deng YP, Jin H, Wang S, Su D, Hu Y, Chen Z. *J Mater Chem A*, 2021, 9: 2325–2333
20 Xu L, Sun Z, Zhu Y, Han Y, Wu M, Ma Y, Huang Y, Zhang H, Chen Y. *Sci China Mater*, 2020, 63: 2435–2442
21 Cui Z, Manthiram A. *Angew Chem Int Ed*, 2023, 62: e202307243
22 Eum D, Jang HY, Kim B, Chung J, Kim D, Cho SP, Song SH, Kang S, Yu S, Park SO, Song JH, Kim H, Tamwattana O, Kim DH, Lim J, Kang K. *Energy Environ Sci*, 2023, 16: 673–686
23 Richards WD, Dacek ST, Kitchaev DA, Ceder G. *Adv Energy Mater*, 2017, 8: 1701533
24 Maslakov KI, Teterin YA, Popel AJ, Teterin AY, Ivanov KE, Kalmykov SN, Petrov VG, Petrov PK, Farnan I. *Appl Surf Sci*, 2018, 448: 154–162
25 Sun Z, Xu L, Dong C, Zhang H, Zhang M, Ma Y, Liu Y, Li Z, Zhou Y, Han Y, Chen Y. *Nano Energy*, 2019, 63: 103887
26 Guo Y, Guo C, Huang P, Han Q, Wang F, Zhang H, Liu H, Cao YC, Yao Y, Huang Y. *eScience*, 2023, 3: 100091
27 Luo D, Zhu H, Xia Y, Yin Z, Qin Y, Li T, Zhang Q, Gu L, Peng Y, Zhang J, Wiaderek KM, Huang Y, Yang T, Tang Y, Lan S, Ren Y, Lu W, Wolverton CM, Liu Q. *Nat Energy*, 2023, 8: 1078–1087
28 Xu P, Shuang ZY, Zhao CZ, Li X, Fan LZ, Chen A, Chen H, Kuzmina E, Karaseva E, Kolosnitsyn V, Zeng X, Dong P, Zhang Y, Wang M, Zhang Q. *Sci China Chem*, 2023, 67: 67–86
29 Jiang Y, Yu F, Que L, Deng L, Xia Y, Ke W, Han Y, Wang Z. *ACS Energy Lett*, 2021, 6: 3836–3843
30 Zhang B, Zhang Y, Wang X, Liu H, Yan Y, Zhou S, Tang Y, Zeng G, Wu X, Liao HG, Qiu Y, Huang H, Zheng L, Xu J, Yin W, Huang Z, Xiao Y, Xie Q, Peng DL, Li C, Qiao Y, Sun SG. *J Am Chem Soc*, 2023, 145: 8700–8713
31 Cui T, Xu J, Wang X, Liu L, Xiang Y, Zhu H, Li X, Fu Y. *Nat Commun*, 2024, 15: 4742
32 Zhang J, Zhang Q, Wong D, Zhang N, Ren G, Gu L, Schulz C, He L, Yu Y, Liu X. *Nat Commun*, 2021, 12: 3071
33 Wang G, Xie C, Wang H, Li Q, Xia F, Zeng W, Peng H, Van Tendeloo G, Tan G, Tian J, Wu J. *Adv Funct Mater*, 2024, 34: 2313672
34 Meng J, Xu L, Ma Q, Yang M, Fang Y, Wan G, Li R, Yuan J, Zhang X, Yu H, Liu L, Liu T. *Adv Funct Mater*, 2022, 32: 2113013
35 Wang X, Zhang Q, Zhao C, Li H, Zhang B, Zeng G, Tang Y, Huang Z, Hwang I, Zhang H, Zhou S, Qiu Y, Xiao Y, Cabana J, Sun CJ, Amine K, Sun Y, Wang Q, Xu GL, Gu L, Qiao Y, Sun SG. *Nat Energy*, 2024, 9: 184–196
36 Li T, Geraci TS, Koirala KP, Zohar A, Bassey EN, Chater PA, Wang C, Navrotsky A, Clément RJ. *J Am Chem Soc*, 2024, 146: 24296–24309
37 Wang R, Weng B, Mahadevegowda A, Temprano I, Wang H, He Z, Ducati C, Xiao Y, Grey CP, De Volder MFL. *Adv Energy Mater*, 2024, 14: 2401097
38 Ni L, Guo R, Fang S, Chen J, Gao J, Mei Y, Zhang S, Deng W, Zou G, Hou H, Ji X. *eScience*, 2022, 2: 116–124
39 Zhao R, Wu M, Jiao P, Wang X, Zhu J, Zhao Y, Zhang H, Zhang K, Li C, Ma Y, Chen Y. *Nano Res*, 2023, 16: 6805–6814
40 Liu X, Li Y, Liu J, Wang H, Zhuang X, Ma J. *Adv Mater*, 2024, 36: 2401505
41 Liu H, Qian D, Verde MG, Zhang M, Baggetto L, An K, Chen Y, Carroll KJ, Lau D, Chi M, Veith GM, Meng YS. *ACS Appl Mater Interfaces*, 2015, 7: 19189–19200
42 Tian JX, Guo HJ, Wan J, Liu GX, Wen R, Wan LJ. *Sci China Chem*, 2023, 66: 2921–2928